Buckling of a stiff film bound to a compliant substrate (part II). A global scenario for the formation of herringbone pattern

Basile Audoly

Institut Jean le Rond d'Alembert, UMR 7190 du CNRS, CNRS/Université Pierre et Marie Curie, 4 place Jussieu, F-75252 Paris Cedex 05

Arezki Boudaoud

Laboratoire de Physique Statistique, UMR 8550 du CNRS/Paris 6/Paris 7 École normale supérieure, 24 rue Lhomond, F-75231 Paris Cedex 05

Abstract

We study the buckling of a thin compressed elastic film bonded to a compliant substrate. We focus on a family of buckling patterns, such that the film profile is generated by two functions of a single variable. This family includes the unbuckled configuration, the classical primary mode made of straight stripes, as well the pattern with undulating stripes obtained by a secondary instability investigated in the first companion paper, and the herringbone pattern studied in last companion paper. A simplified buckling model relevant for the analysis of these patterns is introduced. It is solved analytically for moderate or for large residual compressive stress in the film. Numerical simulations are presented, based on an efficient implementation. Overall, the analysis provides a global picture for the formation of herringbone patterns under increasing residual stress. The film shape is shown to converge at large load to a developable shape with ridges. The wavelength of the pattern, selected in a first place by the primary buckling bifurcation, is frozen during the subsequent increase of loading.

Key words: Buckling, Plates, Thermal stress, Asymptotic analysis, Energy methods

1 Introduction

Buckling of thin plates is a classical subject in engineering mechanics. In particular, the buckling of multi-layered materials has received much attention due to its importance in the design of sandwich panels (Allen, 1969). This field has been the subject of recent work, in connection with the generation of wrinkles in human skin or the templating and assembly of materials (see e.g. Genzer and Groenewold, 2006, for a review). Here, we consider the buckling of a thin and stiff film bonded to a compliant substrate. In typical experiments, thin metallic films are deposited on an elastomer (Bowden et al., 1998; Huck et al., 2000; Yoo et al., 2002). When the system is cooled, compressive residual stress is induced in the film, caused by the mismatch in the thermal expansion coefficients of the two layers. This can lead to buckling into straight wrinkles (Bowden et al., 1998), i. e. to a pattern that is invariant in one direction and has cylindrical symmetry. Other patterns may also appear (see e.g. Audoly and Boudaoud, 2007a). Here we focus on herringbone patterns, also called chevron or zigzag patterns, which have been observed for instance by Huck et al. (2000); in such patterns, the crests and valleys of the wrinkles adopt characteristic zigzag shapes.

Herringbone patterns have been studied numerically. Chen and Hutchinson (2004) simulated the elementary cell of a periodic herringbone pattern, assumed to be a parallelogram; they investigated the dependence of energy on the geometrical parameters of the cell. Huang et al. (2004) undertook simulations on a grid much larger than the wavelength; they first considered the case of a Winkler foundation (a foundation made of linear springs) and later (Huang et al., 2005) the case of a thick elastic foundation. They observed herringbones in either of the following conditions: with isotropic [1] compressive stress when the simulations is initialized with an array of 'nascent' herringbones, or with anisotropic compressive stress and random initialization.

In the first companion paper (Audoly and Boudaoud, 2007a), we investigated the stability of the straight wrinkles (stripe pattern); we found that these wrinkles soon become linearly unstable with respect to a pattern comprising undulating stripes. In the last companion paper (Audoly and Boudaoud, 2007c), herringbones are recovered as a solution of the equations for plates on an elastic foundation, based on an asymptotic analysis in the limit of a large buckling parameter. The present paper aims at bridging the gap between these limits of moderate (first paper) and large buckling parameters (last paper), and shows that undulating stripes evolve smoothly towards herringbones under increasing load. This analysis is based on a simplified buckling

[1] As in the companion papers, 'isotropic' stress is used as a synonym for 'equi-biaxial' and anisotropic' as a synonym for biaxial but not equi-biaxial.

model which, as in Audoly and Boudaoud (2003), addresses the buckling in a well-chosen subspace of configurations for which analytical and numerical solutions can be derived. It provides a global picture of buckling into herringbone patterns under increasing (from small to large) residual stress.

In this paper, our approach is to understand the formation of herringbones at large residual stress, characterized by faceted shapes with sharp folds, and the selection of wavelengths. This involves following the evolution of a particular pattern, not necessarily that with the lowest energy, under increasing loads. We do not include here the patterns that are unrelated to herringbones even if they can be observed at small residual stress — this is the case for checkerboards for instance. They have been the subject of the first companion paper.

The present paper is organized as follows. In Section 2, we briefly recall the formulation of the problem, given in the companion paper (Audoly and Boudaoud, 2007a). In Section 3, we introduce the simplified buckling model which is analyzed in the subsequent sections. In Section 4, we give the results of the linear stability analysis and of the weakly post-buckled analysis based on this approximate model, and compare with the exact results of the first companion paper. In Section 5, we present comprehensive numerical simulations of the model, which allow one to explore moderate to large load. In Section 6, we undertake an asymptotic analysis of the limit of large load, and derive solutions which describes patterns similar to herringbone, found in the preceding numerical analysis. In Section 7, we point out the existence of many local equilibria at large load and discuss the selection of the pattern observed in the experiments.

2 Formulation

We consider an thin elastic film bound to an elastic foundation. The dimensions of the film are infinite in its two in-plane directions. In the following, we write the elastic energy of the system per unit area in the framework of Hookean elasticity, that is assuming a linearly elastic response. The film is loaded with a biaxial, uniform residual stress. We focus on the case of compressive stress, which may make the film unstable. The film is described by the Föppl–von Kármán plate equations with moderate deflections (Timoshenko and Gere, 1961). The foundation is assumed to be an infinitely deep, linearly elastic solid.

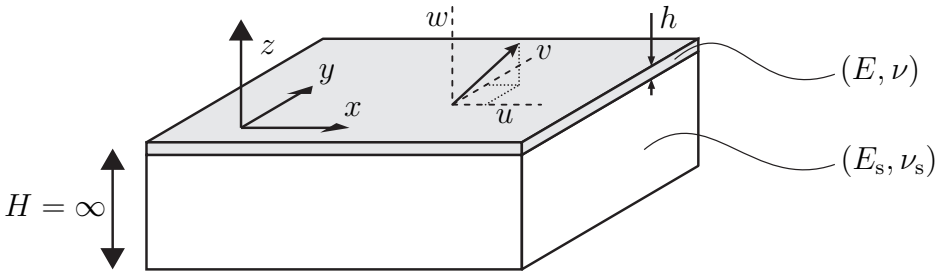

Fig. 1. Geometry of the problem and notations.

2.1 Film

We denote the E, ν and h the Young's modulus, Poisson's ratio and thickness of the film, respectively. The reduced Young's modulus is defined as $E^* = E/(1-\nu^2)$. The loading is given in terms of the differential strain [2] η_x, η_y between film and substrate, the x and y directions being chosen as the principal directions of this differential strain (see Fig. 1 for the geometry and notations). By this, we mean that the residual stress in the film is equivalent to that obtained by starting from the stress-free configurations of the film and substrate, contracting the film by a factor η_x along the x direction and η_y in the y direction, and finally binding the film to substrate. This defines the reference configuration of the system. We are interested in the subsequent deformation of the film and substrate in response to this loading.

We denote $u(x,y)$, $v(x,y)$ and $w(x,y)$ the two components of the in-plane displacements and the out-of-plane displacement of the center-surface of the film, respectively. Then, the film in-plane strain in actual configuration reads:

$$\epsilon_{xx} = -\eta_x + \frac{\partial u}{\partial x} + \frac{1}{2}\left(\frac{\partial w}{\partial x}\right)^2, \tag{1a}$$

$$\epsilon_{xy} = \frac{1}{2}\left(\frac{\partial u}{\partial y} + \frac{\partial v}{\partial x} + \frac{\partial w}{\partial x}\frac{\partial w}{\partial y}\right), \tag{1b}$$

$$\epsilon_{yy} = -\eta_y + \frac{\partial v}{\partial y} + \frac{1}{2}\left(\frac{\partial w}{\partial y}\right)^2. \tag{1c}$$

Using the classical approximations of the Föppl-von Kàrmàn plate theory, nonlinear terms involving the in-plane displacement (u, v) have been neglected. For simplicity, the film material is assumed to be isotropic. The constitutive

[2] Traditionally, the loading is characterized in terms of the residual stress in the film which, from equation (2), are related to the differential strain by $\sigma^0_{xx} = -E\,(\eta_x + \nu\,\eta_y)/(1-\nu^2)$ and $\sigma^0_{yy} = -E\,(\eta_y + \nu\,\eta_x)/(1-\nu^2)$.

equations for the film are those for plane-strain, two dimensional elasticity:

$$\sigma_{xx} = \frac{E}{1-\nu^2}(\epsilon_{xx} + \nu\,\epsilon_{yy}), \tag{2a}$$

$$\sigma_{xy} = \frac{E}{1+\nu}\epsilon_{xy}, \tag{2b}$$

$$\sigma_{yy} = \frac{E}{1-\nu^2}(\epsilon_{yy} + \nu\,\epsilon_{xx}). \tag{2c}$$

The stretching energy per unit area of the film reads

$$\mathcal{E}_{\rm fs} = \frac{1}{L_x\,L_y}\,\frac{h}{2}\int \sigma_{\alpha\beta}\,\epsilon_{\alpha\beta}\,\mathrm{d}x\,\mathrm{d}y, \tag{3}$$

while its bending energy per unit surface is given by the integral of the squared mean curvature:

$$\mathcal{E}_{\rm fb} = \frac{1}{L_x\,L_y}\,\frac{D}{2}\int (\nabla^2 w)^2\,\mathrm{d}x\,\mathrm{d}y, \tag{4}$$

where ∇ denotes the gradient of a function of two variables, (x, y). According to plate theory, the bending modulus is

$$B = \frac{E\,h^3}{12\,(1-\nu^2)}. \tag{5}$$

Finally, we write the total energy of the film per unit area as

$$\mathcal{E}_{\rm f} = \mathcal{E}_{\rm fs} + \mathcal{E}_{\rm fb}. \tag{6}$$

2.2 Substrate

The substrate, which fills the half-space $z < 0$, has Young's modulus $E_{\rm s}$ and Poisson's ratio $\nu_{\rm s}$. The substrate has linear elastic response. Introducing the Fourier transform of the film deflection

$$\hat{w}(k_x, k_y) = \int \mathrm{d}x\ \mathrm{d}y\ w(x,y)\exp[-i(k_x x + k_y y)], \tag{7}$$

the energy of substrate can be written as

$$\mathcal{E}_{\rm s} = \frac{1}{L_x\,L_y}\int \mathrm{d}k_x\ \mathrm{d}k_y\ E_{\rm s}^*\sqrt{k_x^2+k_y^2}\ \hat{w}(k_x,k_y)\hat{w}(-k_x,-k_y). \tag{8}$$

It depends on only one parameter $E_{\rm s}^*$, which is proportional to $E_{\rm s}$ and is a function of Poisson's ratio $\nu_{\rm s}$,

$$E_{\rm s}^* = \frac{E_{\rm s}\,(1-\nu_{\rm s})}{(1+\nu_{\rm s})\,(3-4\nu_{\rm s})}. \tag{9}$$

For details, we refer to the first companion paper (Audoly and Boudaoud, 2007a).

2.3 Optimization problem

The goal of the paper is to derive equilibrium solutions describing buckled states. This involves minimizing the total energy, which is the sum of the film and substrate energies:

$$\mathcal{E}_{\mathrm{t}}(\{u,v,w\}) = \mathcal{E}_{\mathrm{s}}(\{w\}) + \mathcal{E}_{\mathrm{f}}(\{u,v,w\}). \tag{10}$$

This energy has to be minimized with respect to the three components of the film's displacement,

$$(u(x,y), v(x,y), w(x,y)),$$

for given values of the material parameters and differential strain (η_x, η_y).

3 A simplified model for the analysis of buckling

As explained in the introduction, the first companion paper is concerned with small to moderate residual stress, and the last one with large stress. In the present one, we discuss the case of intermediate loading. In particular, we study the selection of the herringbone pattern and its wavelength. This question is of particular importance as we shall see that global energy minimization does not provide a consistent selection mechanism. The general question we address here is how undulating stripe patterns evolve when the differential strain is progressively increased from the initial buckling threshold to much larger values. This progressive increase of the loading does take place in typical experiments, whereby a sample obtained at high temperature cools down progressively.

Pattern selection is difficult to approach based solely on numerical simulations (as in Huang et al., 2004, 2005) as it is impossible to vary systematically all the parameters of the problem. Moreover, the final pattern depends largely on the arbitrary initial condition. On the analytical side, we have exhausted in the two companion papers all the methods that allow for exact results, by exploiting the presence of a small parameter in the limits of small or large load. In contrast, no analytical solution for the buckling problem formulated in Section 2 is available in the case of intermediate load. For this reason, we introduce a simplified buckling model. It is designed in such a way that the essential features of the original model are retained; on the other hand, is simple enough that it can be studied analytically and simulated very efficiently.

3.1 Motivation

To introduce our simplified model, we shall first list the various exact solutions that can be derived for the film shape, for different values of the residual stress. The first ones are the unbuckled solution, below the initial threshold, and the cylindrical mode (stripes) just above it:

$$w(x,y) = 0 \tag{11a}$$
$$w(x,y) = A\,\cos(k\,x), \tag{11b}$$

where A is the amplitude of the mode and k the wavenumber. These classical solutions are recalled in the first companion paper. The undulating stripe pattern, introduced in the same paper, is another solution valid slightly above the secondary threshold, which we rewrite as follows:

$$\begin{aligned} w(x,y) &= A\,\cos(k\,x) + b\,\sin(k\,x)\,\sin(k\,q\,y) \\ &\simeq A\,\cos\left[k\,\left(x - \frac{b\,\sin(k\,q\,y)}{k\,A}\right)\right] + \mathcal{O}\left(\frac{b^2}{A}\right). \end{aligned} \tag{11c}$$

Here, b is the amplitude of the perturbation to the cylindrical model, and $b \ll A$ slightly above threshold; q defines the aspect ratio of the pattern, that is the ratio of the longitudinal and transverse wavenumbers.

Another analytical solution, derived in the last companion paper for large differential strain, is the Miura-ori pattern, defined by

$$w(x,y) = A\,S\left(\frac{x + a\,\tan\theta\left(\frac{1}{2} + S\left(\frac{y}{a} - \frac{1}{2}\right)\right)}{b}\right), \tag{11d}$$

where a and b now define the dimensions of the unit cell of this periodic pattern.

We now formulate a key remark: for all the analytical solutions in equations (11a–11d), the deflection $w(x,y)$ is of the form:

$$w(x,y) = f(x - g(y)), \tag{12}$$

for some functions f and g that depend on the profile considered (see Fig. 2). Indeed, for the unbuckled configuration, $f(x) = 0$ and g is arbitrary; for the straight stripes, $f(x) = A\,\cos(kx)$ and $g(y) = 0$; for the undulating stripe pattern, $f(x) = A\,\cos(kx)$ and $g(y) = b\,\sin(kqy)/(kA)$: for the Miura-ori (herringbone) pattern, $f(x) = A\,S(x/b)$ and $g(y) = -a\,\tan\theta\,(1/2 + S(y/a - 1/2))$.

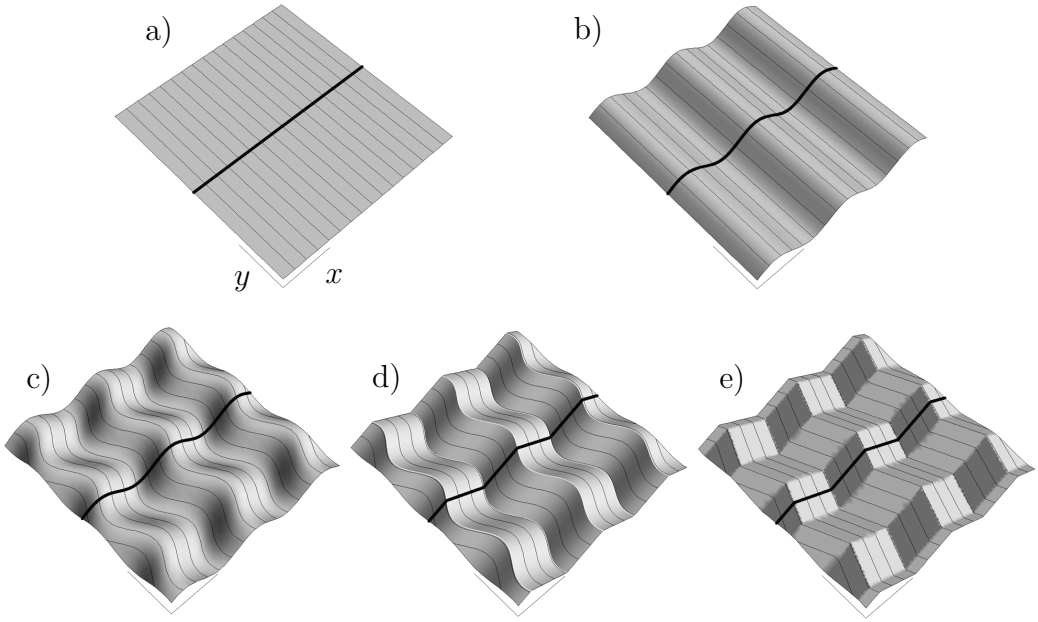

Fig. 2. All the patterns derived so far belong the class of quasi-1D patterns, as defined in equation (13a). (a) unbuckled, $f(x) = 0$ $g(y) = 0$; (b) straight stripes (cylindrical pattern), $f(x) = .7\cos x$, $g(y) = 0$; (c) undulating stripes, $f(x) = .7\cos x$, $g(y) = .6\sin y$; (d) developable surface with curvilinear ridges $f(x) = .8\,S(x)$, $g(y) = .6\sin y$; (e) herringbone pattern (also called Miura-ori and zigzag pattern), $f(x) = .8\,S(x)$, $g(y) = .7\,(1/2 + S(y - 1/2))$.

3.2 Kinematical constraints

Our aim is to study the transition from a flat pattern to straight or undulating stripes at small strain, and to a herringbone (Miura-Ori) pattern at large strain. Since all these patterns are of the particular form $w(x, y) = f(x - g(y))$, we propose to analyze the evolution of the pattern under increasing loading within this reduced space of configurations. In other words, we suggest to *constrain* the profile to be of the form $w(x, y) = f(x - g(y))$, even at intermediate load values. This approximation provides a workaround to the absence of analytical solutions to the full problem. It is natural given the particular form of the various exact solutions.

Technically, we consider the buckling problem as a minimization problem within a reduced space of configurations, which we call *quasi-1D* configurations. This space is defined as

$$\mathcal{Q} = \{w(x, y) \mid w(x, y) = f(x - g(y))\}\,, \tag{13a}$$

where the vertical bar stands for 'such that'. It has already been emphasized that the planar, cylindrical, undulating stripes and Miura-Ori patterns all belong to this class. Within this class, the deflection is no longer an arbitrary

function of two variables. Instead, it is fully specified by two functions f and g of a single variable. As a result, the Euler-Lagrange equations associated with the condition of energy minimum takes the form of coupled *ordinary* differential equations for f and g in the quasi-1D problem, instead of partial differential equations in the original problem. In numeric calculations, the number of degrees of freedom is $(2\,N)$ for a grid of size $N \times N$, instead of (N^2).

Even with the previous approximation, the Euler-Lagrange equations expressing the condition of energy minimum are not solvable analytically because the in-plane displacements $u(x, y)$ and $v(x, y)$ are required in addition to the deflection $w(x, y)$. In order to avoid this difficulty, we shall further constrain the kinematics of the film and seek solutions within the class $\mathcal{Q} \cap \mathcal{R}$, where

$$\mathcal{R} = \{u(x, y), v(x, y), w(x, y) \mid \nabla\epsilon_{xx} = 0 \;\&\; \epsilon_{xy} = 0\}\,, \tag{13b}$$

the strain being defined in terms of the displacement by equation (1). In this class, the film has uniform strain component ϵ_{xx} and a vanishing in-plane shear strain [3]. This approximation was successfully used for the analysis of multiscale, self-similar buckling patterns (Audoly and Boudaoud, 2003). It is a reasonable approximation for studying the evolution of the system under increasing load; indeed, developable surfaces, such that $\epsilon_{\alpha\beta} = 0$ for α and $\beta = x, y$, belong to the class $\mathcal{R}$ by definition, those developable solutions being the preferred solutions of the original problem at large compressive stress. Because of this, we avoid the difficulties associated with another popular but much cruder approximation that consists in setting to zero the in-plane displacements (see Jin and Sternberg, 2001, for a discussion of the drawbacks of such models).

We do not claim that the two approximations $\mathcal{Q}$ and $\mathcal{R}$ just proposed can be justified rigorously. As a matter of fact, solutions of the simplified problem are not solutions of the original problem and we do not expect the simplified analysis of buckling that follows to agree in full details with that based on the original theory. Our assumptions are merely a set of convenient and reasonable approximations that allow for analytical calculations and fast numerical simulations, provide good insights into the phenomena and capture the main features of transition towards herringbone patterns. This view is supported by the analysis of Section 4, where the analyses carried out in the first companion paper on the full model is repeated, with similar results, on the quasi-1D model.

[3] This class $\mathcal{R}$ treats differently the two in-plane directions x and y, as ϵ_{yy} may well be nonzero. The resulting model is not covariant with respect to in-plane rotations. This is not really a problem as the quasi-1D patterns $\mathbf{Q}$ that we consider are not isotropic anyway.

We shall first show that, using the kinematical hypothesis $\mathcal{R}$, the in-plane displacements u and v can be reconstructed from the deflection w. The constrain that the strain component ϵ_{xx} is uniform can be rewritten as $\epsilon_{xx}(x,y) = \langle \epsilon_{xx} \rangle$. Here and later, the brackets $\langle \cdot \rangle$ stand for the average over x and y of the quantity inside, whereas the brackets $\langle \cdot \rangle_x$ denote the average in the x direction only. This allows one to express u from equation (1a) as

$$\begin{aligned} \frac{\partial u}{\partial x} &= \langle \epsilon_{xx} \rangle + \eta_x - \frac{1}{2} \left(\frac{\partial w}{\partial x} \right)^2 \\ &= \langle \epsilon_{xx} \rangle + \eta_x - \frac{1}{2} f'^2(x - g(y)) \end{aligned} \tag{14}$$

Let $F(x)$ be the antiderivative of $(f'^2(x) - \langle f'^2 \rangle)$ with a constant of integration chosen such that F is zero on average:

$$F'(x) = f'^2(x) - \left\langle f'^2 \right\rangle \text{ and } \langle F \rangle = 0. \tag{15}$$

In the absence of ambiguity, the averages of functions of the variable x only, such as $\langle f'^2 \rangle$, are noted $\langle \cdot \rangle$ or $\langle \cdot \rangle_x$ indifferently.

By integration along x of equation (14) for $\partial u / \partial x$, one obtains

$$u(x,y) = \left(\langle \epsilon_{xx} \rangle + \eta_x - \frac{1}{2} \left\langle f'^2 \right\rangle \right) x - \frac{1}{2} F(x - g(y)) + \phi(y),$$

where ϕ is an arbitrary function of y. Now, $u(x,y)$ has to a bounded function for the substrate energy to remain finite. Therefore, the prefactor of x in the expression above has to vanish:

$$\langle \epsilon_{xx} \rangle = -\eta_x + \frac{1}{2} \left\langle f'^2 \right\rangle, \tag{16}$$

which leads to

$$u(x,y) = -\frac{1}{2} F(x - g(y)) + \phi(y). \tag{17}$$

Having computed $u(x,y)$, we can now obtain $v(x,y)$ by plugging the kinematical assumption $\epsilon_{xy}(x,y) = 0$ into equation (1b):

$$\begin{aligned} \frac{\partial v}{\partial x} &= -\frac{\partial u}{\partial y} - \frac{\partial w}{\partial x} \frac{\partial w}{\partial y} \\ &= -\frac{1}{2} g'(y) F'(x - g(y)) - \phi'(y) + g'(y) f'^2(x - g(y) \\ &= \frac{1}{2} g'(y) F'(x - g(y)) + \langle f'^2 \rangle g'(y) - \phi'(y). \end{aligned}$$

As for u, the displacement v has to be bounded and this implies that the averaged derivative of v with respect to x is zero: $\langle \partial v/\partial x \rangle_x = 0$. This yields, using $\langle F' \rangle = 0$ and $\langle g' \rangle = 0$ (as $g(y)$ is periodic hence bounded):

$$\phi'(y) = \langle f'^2 \rangle \, g'(y).$$

We have averaged over the variable x only to obtain this equation. Plugging back the above expression for ϕ' into the expression for $\partial v/\partial x$ and carrying out the integration with respect to x, one obtains $v(x, y)$ as

$$v(x, y) = \frac{1}{2} \, g'(y) \, F(x - g(y)) + \psi(y), \tag{18}$$

where ψ is another arbitrary function, to be determined.

3.4 Energy

Having determined the displacement, we can compute the strain. The component ϵ_{xx}, which is constant by construction, has already been given in equation (16). The shear component is zero by construction. The remaining component, ϵ_{yy}, can be computed from equation (1c). This yields:

$$\epsilon_{xx}(x, y) = -\eta_x + \left\langle \frac{f'^2}{2} \right\rangle \tag{19a}$$

$$\epsilon_{xy}(x, y) = 0 \tag{19b}$$

$$\epsilon_{yy}(x, y) = -\eta_y + \frac{1}{2} \langle f'^2 \rangle \, g'^2(y) + \frac{1}{2} \, g''(y) \, F(x - g(y)) + \psi'(y). \tag{19c}$$

Anticipating the rest of the calculation, we decompose the last component into three contributions,

$$\epsilon_{yy}(x, y) = \epsilon^{(1)}_{yy}(x, y) + \epsilon^{(2)}_{yy}(y) + \epsilon^{(3)}_{yy}, \tag{20}$$

defined by

$$\epsilon^{(1)}_{yy}(x, y) = \epsilon_{yy}(x, y) - \langle \epsilon_{yy}(x, y) \rangle_x \tag{21a}$$

$$\epsilon^{(2)}_{yy}(y) = \langle \epsilon_{yy}(x, y) \rangle_x - \langle \epsilon_{yy} \rangle \tag{21b}$$

$$\epsilon^{(3)}_{yy} = \langle \epsilon_{yy} \rangle. \tag{21c}$$

By construction, these quantities satisfy

$$\langle \epsilon^{(1)}_{yy}(x, y) \rangle_x = 0 \text{ for all } y, \text{ and } \langle \epsilon^{(2)}_{yy}(y) \rangle_y = 0, \tag{22}$$

which in particular implies $\langle \epsilon_{yy}^{(1)}(x,y)\rangle = \langle \epsilon_{yy}^{(2)}(x,y)\rangle = 0$. From equation (19c), one can find explicit expressions for these three terms:

$$\epsilon_{yy}^{(1)}(x,y) = \frac{1}{2}\, g''(y)\, F(x - g(y)) \tag{23a}$$

$$\epsilon_{yy}^{(2)}(y) = \frac{1}{2}\, \langle f'^2\rangle\, (g'^2(y) - \langle g'^2\rangle) + \psi'(y) \tag{23b}$$

$$\epsilon_{yy}^{(3)} = -\eta_y + \frac{1}{2}\, \langle f'^2\rangle\, \langle g'^2\rangle. \tag{23c}$$

Indeed, one can notice that $\langle \psi'\rangle = 0$, as implied by the equality $\langle \partial v/\partial y\rangle = 0$ which comes itself from the fact that the displacement $v(x,y)$ is bounded.

With the aim to formulate a minimization problem with respect to the two unknown functions $f(x)$ and $g(y)$ and the auxiliary function $\psi(y)$, we compute the stretching the energy per unit area of the film, defined by equations (2a–2c) and (3) in terms of the strain tensor:

$$\mathcal{E}_{\text{fs}}(\{u,v,w\}) = \frac{Eh}{2(1-\nu^2)}\, \frac{1}{L_x\, L_y} \int \mathrm{d}x\, \mathrm{d}y\, (\epsilon_{xx}^2 + \epsilon_{yy}^2 + 2\nu\, \epsilon_{xx}\epsilon_{yy}).$$

When the decomposition (20) for ϵ_{yy} is plugged into this expression, all the cross-products of the form $(\epsilon_{yy}^{(i)}\, \epsilon_{yy}^{(j)})$, with $i \neq j$ vanish upon integration due to equation (22). This leads to the following expression for the film stretching energy:

$$\mathcal{E}_{\text{fs}}(\{u,v,w\}) = \\ \frac{Eh}{2(1-\nu^2)} \left(\langle \epsilon_{xx}\rangle^2 + \langle (\epsilon_{yy}^{(1)})^2\rangle + \langle (\epsilon_{yy}^{(2)})^2\rangle + (\epsilon_{yy}^{(3)})^2 + 2\nu\, \langle \epsilon_{xx}\rangle\, \langle \epsilon_{yy}\rangle\right). \tag{24}$$

Here, the last term has been rewritten using the following equalities:

$$\frac{1}{L_x\, L_y} \int \mathrm{d}x\, \mathrm{d}y\, \epsilon_{xx}\, \epsilon_{yy} = \langle \epsilon_{xx}\, \epsilon_{yy}\rangle = \langle \langle \epsilon_{xx}\rangle\, \epsilon_{yy}\rangle = \langle \epsilon_{xx}\rangle\, \langle \epsilon_{yy}\rangle,$$

since ϵ_{xx} is uniform by construction.

In the stretching energy (24), the function ψ enters via a single term, namely $\langle (\epsilon_{yy}^{(2)})^2\rangle^2$, whose value is given by equation (23b). Therefore, the optimality condition of the stretching energy with respect to this function ψ, which writes formally as

$$\frac{\delta \mathcal{E}_{\text{fs}}}{\delta \psi'(y)} = 0,$$

leads to

$$\epsilon_{yy}^{(2)}(y) = 0.$$

This equation allows one to determine the auxiliary function ψ,

$$\psi'(y) = -\frac{1}{2}\, \langle f'^2\rangle\, (g'^2(y) - \langle g'^2\rangle).$$

We can finally write the stretching energy of the film for our reduced model by combining the equations above:

$$\mathcal{E}_{\mathrm{fs}}(w \in \mathcal{Q} \cap \mathcal{R}) = \frac{Eh}{2\left(1-\nu^2\right)} \left(\frac{\langle g''^2 \rangle \langle F^2 \rangle}{4} + \left(\frac{\langle f'^2 \rangle}{2} - \eta_x \right)^2 + \left(\frac{\langle f'^2 \rangle \langle g'^2 \rangle}{2} - \eta_y \right)^2 + 2\nu \left(\frac{\langle f'^2 \rangle}{2} - \eta_x \right) \left(\frac{\langle f'^2 \rangle \langle g'^2 \rangle}{2} - \eta_y \right) \right), \quad (25)$$

where the function F is defined by equation (15). Thanks to our kinematical assumptions, we have been able to write the film stretching energy in a simple, closed form.

The other contributions to the energy are the film's bending energy and the substrate energy. The bending energy can be computed by plugging the special form of $w(x, y)$ given in equation (13a) into equation (4). This yields

$$\mathcal{E}_{\mathrm{fb}}(w \in \mathcal{Q}) = \frac{D}{2} \Big(\langle [1 + g'^2(y)]^2 \rangle \langle f''^2(x) \rangle + \langle g''^2 \rangle \langle f'^2 \rangle - \frac{2}{L_x L_y} [g' + g'^3/3]_0^{L_y} [f'^2/2]_0^{L_x} \Big). \quad (26)$$

The last two terms are boundary terms, which vanish when f and g are assumed to be periodic and continuous, which is what we do in the simulations.

The substrate energy $\mathcal{E}_{\mathrm{s}}(w \in \mathcal{Q})$, defined by equation (8), cannot be found explicitly in terms of f and g. In the numerical simulations, it is computed by a two dimensional Fourier transform of the profile $w(x, y) = f(x - g(y))$. For the analyses of stability of Section 4, this substrate energy is computed by expansion near the bifurcation threshold.

We have derived a simplified model for the analysis of patterns in stiff films bonded to a compliant substrate. In this model, the total energy is the sum of the film stretching energy (25), the film bending energy (26), and the substrate energy defined by equation (8) with a deflection of the form (12):

$$\mathcal{E}_{\mathrm{t}}(w \in \mathcal{Q} \cap \mathcal{R}) = \mathcal{E}_{\mathrm{fs}}(w \in \mathcal{Q} \cap \mathcal{R}) + \mathcal{E}_{\mathrm{fb}}(w \in \mathcal{Q}) + \mathcal{E}_{\mathrm{s}}(w \in \mathcal{Q}) \quad (27)$$

To study this reduced model, we shall now consider the problem of minimizing this energy with respect to the two functions $f(x)$ and $g(y)$, for different values of the differential strain (η_x, η_y).

4 Linear stability and weakly nonlinear analyses

With the aim to validate our simplified model, we repeated the weakly nonlinear analyses carried out in the companion paper, which are relevant for small loading, with the aim to compare to the results of the exact model.

4.1 Primary buckling bifurcation

Let us first consider the linear stability analysis of the unbuckled state. We use the same rescalings as in the companion paper, and define

$$h^* = \frac{h}{\sqrt{12\,(1-\nu^2)}}$$

as a unit of length. The stiffness contrast between the two layers reads

$$C = \frac{E^*\,h}{E_{\rm s}^*\,h^*}. \tag{28}$$

This large number is used to rescale the differential strain:

$$\overline{\eta_x} = \frac{\eta_x}{C^{-2/3}}, \quad \overline{\eta_y} = \frac{\eta_y}{C^{-2/3}}. \tag{29}$$

For the sake of brevity, we shall not give the details of the the analysis of linear stability, which is a classical method. The optimal film shape predicted by the simplified model from equation (27) bifurcates from planar to buckled state above a critical differential strain. The buckled state is characterized by a harmonic profile $w(x,y)$ with amplitude A and wavenumber k satisfying:

$$\begin{aligned} w(x,y) &= A\,\cos(kx) \\ A &= 2h\,\sqrt{\overline{\eta}_x + \nu\,\overline{\eta}_y - 3(1-\nu^2)} \\ kh^* &= C^{-1/3}. \end{aligned} \tag{30}$$

The planar state becomes linearly unstable when the argument of the square root defining the amplitude A becomes positive. As in the companion paper, the initial buckling threshold under isotropic loading is noted

$$\overline{\eta}_{\rm c}^I = 3\,(1-\nu)$$

Remarkably, the primary instability (30) predicted by the simplified model is identical to that predicted by the full model (see Audoly and Boudaoud, 2007a). In both cases, the buckled state involves a harmonic perturbation of

the film with cylindrical symmetry; the instability threshold, and the amplitude and wavenumbers of the unstable mode are identical. It may be surprising that the analysis of linear stability based on the approximate model allows one to recover the exact results. The reason is that the simplifying kinematical assumptions $\mathcal{Q}$ and $\mathcal{R}$ hold both for the planar state, and for cylindrical stripe pattern immediately above the primary threshold [4].

4.2 Secondary buckling bifurcation

Having studied the initial buckling bifurcation, we can analyze the secondary bifurcations similarly. In the companion paper, this has been done based on the exact equations and we found that a secondary instability leads to undulating stripes; this secondary instability takes place:

- strictly above the initial buckling threshold under anisotropic loading (namely when either η_x or η_y reaches η_c^I),
- concomitantly with the initial buckling under isotropic loading.

Here again, we shall not give the details of the analysis of linear stability of the stripe pattern based on the quasi-1D model. The outcome of this analysis is that straight wrinkles become linearly unstable with respect to undulating stripes too. This secondary instability takes place at a threshold, denoted $\eta_c'^I$ in the isotropic case, which is always strictly above the initial threshold: $\eta_c'^I > \eta_c^I$. The different predictions regarding these thresholds is apparent from Fig. 3. We conclude that the analysis of the secondary bifurcation based on the simplified model is approximate, unlike that of the primary bifurcation. The reason is that the solution describing undulating stripe pattern in the original model does not satisfy the kinematical hypothesis $\mathcal{R}$. There are fewer potentially unstable modes in the quasi-1D model as only those compatible with the kinematical assumptions are available; as a result, the buckling threshold is overestimated in the quasi-1D model. This discrepancy is in fact minor, for two reason: first, we qualitatively recover the same type of secondary instability, leading to undulating stripes; second, the undulating stripes is actually the optimal shape of the quasi-1D model just above the primary buckling threshold η_c^I, although this is not apparent from the present linear stability analysis (see end of Section 5).

[4] This is not a coincidence: the main motivation for the quasi-one dimensional deflection, of the form (12), that is encompasses analytical solutions for the film profile, which includes the cylindrical pattern.

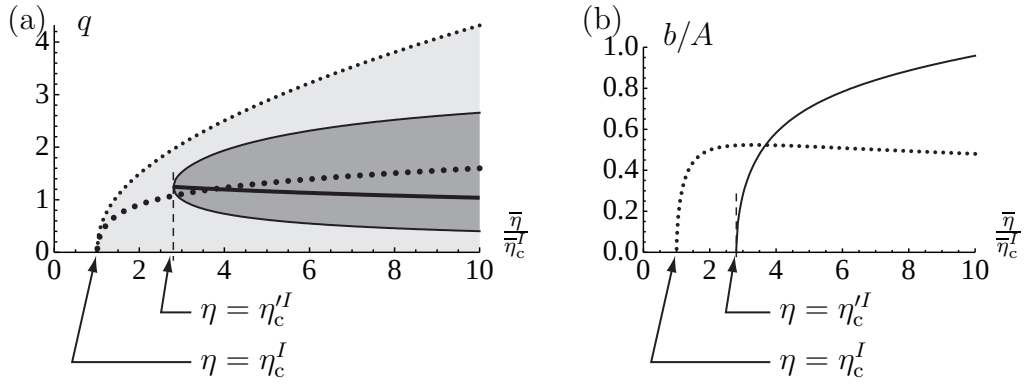

Fig. 3. Linear stability analysis of the cylindrical pattern with respect to zigzags: comparison of the predictions of the approximate quasi-1D model (solid curves) with the exact result (dotted curves) from Audoly and Boudaoud (2007a). (a) Linearly unstable longitudinal wavenumber q (dark grey region) and most unstable wavenumber q (thick curve). (b) Rescaled amplitude b/A of the zigzag perturbation. Both plots are made with Poisson's ratio $\nu = 0.3$.

4.3 Post-buckling analysis

These analysis of linear stability can be complemented by the nonlinear analysis of post-buckled undulating stripes. The results, based on either the full or the quasi-1D model, are compared in Fig. 3. For the sake of brevity, we omit the details of the calculations for the quasi-1D model, which are similar to those for the full model obtained by Audoly and Boudaoud (2007a).

Although the simplified model does not yield exact predictions for the secondary instability threshold, it captures the most salient features of the system: the existence of a primary bifurcation leading to a stripe pattern and of a secondary bifurcation leading to undulating stripes are captured correctly. The thresholds and amplitudes relevant for the primary bifurcations are exact, although those for the secondary bifurcations are approximate (and comparable to the exact ones). This validates our suggestion to use the quasi-1D model as a toy model for analyzing the buckling of a stiff film bonded to a compliant substrate. This is the aim of the rest of the paper, where buckling is investigated under intermediate to large loads.

5 Numerical simulations

The quasi-1D model is first studied numerically, at intermediate loads: we assume the differential strain to be significantly larger — but not larger by orders of magnitude — than the primary and secondary thresholds η_c^I and $\eta_c'^I$. In the absence of analytical methods of solution applicable to this situation,

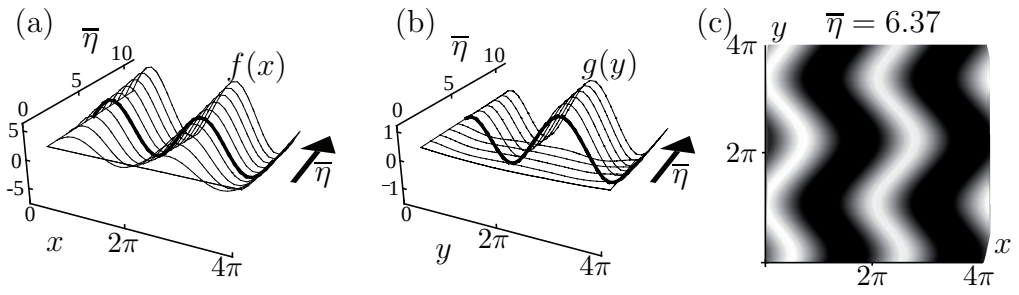

Fig. 4. A typical simulation session of the quasi-1D model, for increasing values of dimensionless load $\overline{\eta}$ (bold arrows). (a) Numerical solutions $f(x)$ and (b) $g(y)$ for different values of $\overline{\eta}$. (c) Visualization of the deflection $w(x, y) = f(x - g(y))$ for a particular value of $\overline{\eta} = 6.37$, corresponding to the thick curves $f(x)$ and $g(y)$ in (a) and (b). The simulation extends over $(\overline{x}, \overline{y}) \in [0, \overline{L}_x] \times [0, \overline{L}_y]$ with $\overline{L}_x = \overline{L}_y = 4\pi$, and is for isotropic load.

we resort to numerical simulations.

5.1 Implementation

The energy of the quasi-one dimensional model (27) is minimized with respect to the values of the functions $f(x)$ and $g(y)$ discretized on even meshes, each having a number of points that is a power of 2, in the range 64–256. The stretching and bending energy of the film, given by equations (25) and (26), are computed using finite differences. The energy of the substrate (8) is computed using a Fast Fourier transform algorithm (FFT). The energy is then minimized by the method of conjugate gradient descent. The size $L_x \times L_y$ of the squared simulation cell is chosen at the beginning of the simulation. Using periodic boundary conditions, we effectively simulate an infinite array of such elementary cells. Ideally, our simulation cell is much larger than the expected size of the buckling pattern, which is of order 2π in dimensionless units (recall that the wavenumber of the primary instability is 1 in dimensionless units); in some cases, especially when using a fine spatial discretization, the actual dimensions of the simulation cell had to be lowered to values comparable to wavelength of the buckling pattern in order to keep the simulation time reasonable. We used rescaled quantities in all the numerical simulations, thereby avoiding to introduce unnecessary errors caused by machine accuracy.

In our simulations, we focused on the case of isotropic differential strain, $\overline{\eta} = \overline{\eta_x} = \overline{\eta_y}$. Then, the only control parameter in the simulation is the rescaled differential strain, $\overline{\eta}$. The result of a typical simulation session is shown in Fig. 4. The functions f and g are initialized with very small, random values. Starting from $\overline{\eta} = 0$, we progressively increase the differential strain, and observe the profiles of the numerical minimizers $f(x)$ and $g(y)$. As explained earlier, the kinematical assumptions in the model allow for offline,

symbolic calculations of the in-plane displacement. The calculations that remain to be done online are essentially the calculation of integrals involving f, g, their derivatives and powers, which is effectively a one-dimensional problem [5], and can be done very quickly, at an interactive rate on a standard personal computer. This makes it quite easy to track solutions under increasing or decreasing loading, and to discriminate between continuous and discontinuous bifurcations, as reported in the end of the present Section.

5.2 Results

In the simulation shown in Fig. 4, we first observe the unbuckled state for low differential strain: $f(x) \approx 0$ for all x and $g(y) \approx 0$ for all y. When $\overline{\eta}$ is increased above a primary threshold, the function f starts to make undulations, although the profile $g(y)$ remains flat. This corresponds to the stripe pattern. At a secondary threshold, the function g starts to make undulations, producing undulating stripes. The values of the thresholds, amplitudes and wavelength are studied in details next, see Fig. 5. They are consistent with the analytical predictions of Section 4. When the loading is further increased, the function f changes progressively from a sinusoidal to a non-smooth, sawtooth-like shape.

In Fig. 5, we present a more detailed analysis of the simulation results, for $\nu = 0.3$. When the loading is increased, starting from $\overline{\eta} = 0$, the unbuckled pattern, characterized by $\langle f'^2 \rangle = 0$ and $\langle g'^2 \rangle = 0$ is first observed. At a threshold very close to that predicted by the theory, $\overline{\eta} = \overline{\eta}_{\rm c}^I = 3\,(1-\nu) = 2.1$, the function $f(x)$ bifurcates. This corresponds to the emergence of a stripe pattern, set inset (B), with a wavelength, 2π in rescaled units, consistent with that predicted by the linear stability analysis. The *squared* amplitude of the pattern, $\langle f'^2 \rangle$, is found to vary linearly with the distance to threshold $\eta - \eta_{\rm c}^I$; this is characteristic of a supercritical (continuous) bifurcation. This is all in agreement with the results of the previous section and with those of the exact model given in the first companion paper (Audoly and Boudaoud, 2007a).

The stripe pattern persists until a secondary threshold is reached. This threshold is very close to the threshold, $\overline{\eta}_{\rm c}'^I(\nu = .3) = 5.88$, predicted by linear stability analysis of the straight wrinkles, see Section 4. This secondary bifurcation turns out to be subcritical (discontinuous): both the energy and the number $\langle g'^2 \rangle$ change by a finite amount in a single simulation step. Above

[5] At every step in the minimization, we need to reconstruct the 2D profile of the plate using equation (12) before we can carry out the fast Fourier transform numerically. This is the only operation that is two-dimensional, *i. e.* that involves N^2 operations where N is the number of discretization points). Being based on a highly optimized algorithm, the fast Fourier transform, it remains very quick and did not slow noticeably the calculation down.

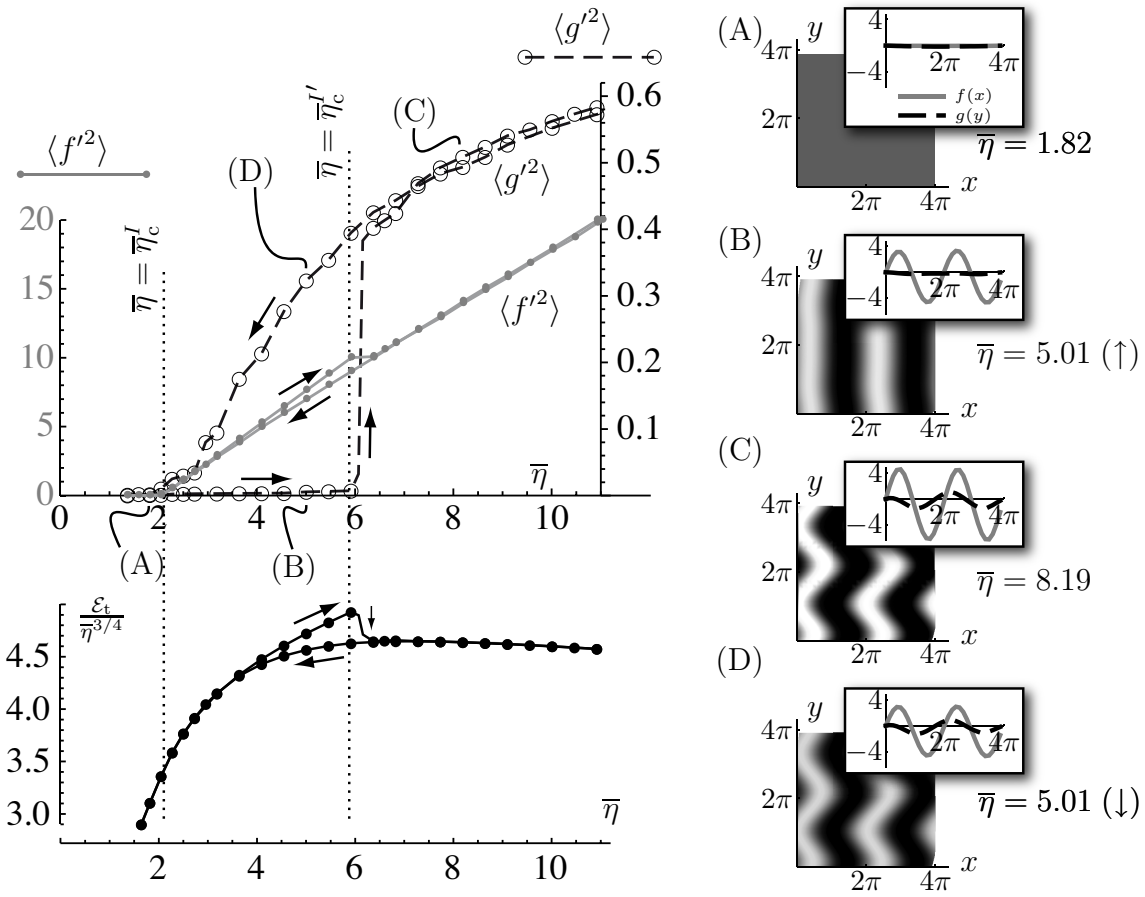

Fig. 5. Simulations based on the quasi-1D model. In the upper-left part of the diagram, the quantities $\langle f'^2\rangle$ and $\langle g'^2\rangle$ are given as a function of the control parameter η, which is first increased and then decreased. Two bifurcations, involving f first and then g, take place very close to the theoretical thresholds (vertical dotted lines). A hysteresis curve is followed when the loading is first increased and then decreased. In the lower left diagram, the energy of the solution is plotted. On the right-hand sides, the 3D configurations of a few representative configurations are shown. The rectangular simulation cell has dimensions $\overline{L}_x = \overline{L}_y = 4\pi$ and resolution $N_x = N_y = 32$. Poisson's coefficient is $\nu = 0.3$.

the secondary threshold, undulating stripes are obtained; the evolution of this pattern when the loading is further increased is analyzed in the next section.

When the loading is subsequently decreased, the solution follows a hysteresis cycle. Below $\overline{\eta}_c'^I$ (but above $\overline{\eta}_c^I$), the film pattern is still given by undulating stripes, although it was made of straight stripes during the loading stage in the same range of differential strain. The energy profile at the bottom of Fig. 5 reveals that the undulating pattern has a lower energy than the straight stripes. In retrospect, it appears that the system has remained trapped in a local minimum of energy in the range $\overline{\eta}_c^I < \overline{\eta} < \overline{\eta}_c'^I$ and under increasing loading, which it could not escape until this local energy minimum became linearly unstable, at $\overline{\eta}_c'^I$.

These numerical results are in complete agreement with the analysis of the simplified model presented in the previous section. Furthermore, the numerical observation of a hysteresis cycle mitigates the main discrepancy found between the exact model and the simplified one. Recall that, with the exact model under isotropic isotropic loading, straight stripes become linearly unstable immediately above the initial buckling threshold $\overline{\eta}_{\mathrm{c}}^{I}$, although in the quasi-1D model they were found to remain linearly stable over a range $\overline{\eta}_{\mathrm{c}}^{I} < \overline{\eta} < \overline{\eta}_{\mathrm{c}}^{\prime I}$ which extends much beyond the initial buckling threshold. As revealed by the numerics, undulating stripe patterns are actually present in the quasi-1D model immediately above the initial threshold too, and are indeed the state of lowest energy — however, they are not accessible by the analysis of linear stability as they appear by a discontinuous bifurcation.

6 Analytical and numerical solution in the limit of large load

Numerical simulations have confirmed the emergence of an undulating pattern by a sequence of two bifurcations, namely an initial bifurcation towards a cylindrical pattern and a secondary bifurcation leading to undulations. In the present section, we investigate how this pattern evolves when residual stress is further increased. We show in details how the pattern, emerging in a first place as a small amplitude perturbation on top of the straight stripe pattern, evolves progressively towards a developable shape with crests and valleys comprising angular points. We shall also address the selection of the wavelengths of the pattern obtained at large differential strain, a question which has remained unsettled so far.

6.1 Penalization of the stretching energy

We shall show that the quasi-1D model can be solved analytically in limit of large differential strain, $\overline{\eta}_x \gg 1$ and $\overline{\eta}_y \gg 1$. As explained before, this model is based on approximations but is expected to provide good insights into the behavior of the full model — in the last companion paper, we discuss in detail the similarities and differences of the predictions of the two models for large load. Note that, by large differential strain, we mean large *rescaled* differential strain $\overline{\eta}_\alpha = \eta_\alpha / C^{-2/3} \gg 1$. The stiffness contrast C is a large number by assumption and so the rescaled strain can be large although the physical strain remains small; in fact, this happens when

$$1 \ll \overline{\eta}_\alpha \ll C^{2/3}. \tag{31}$$

In this regime, it is consistent to use the assumption of a linear elastic response for the substrate and the Föppl-von Kàrmàn equations for the film. In the rest

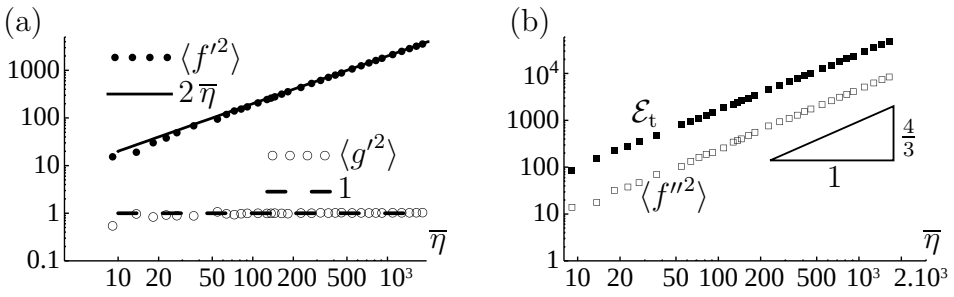

Fig. 6. Numerical confirmation of the scaling laws for $\langle f'^2\rangle$, $\langle g'^2\rangle$, $\langle f''^2\rangle$, and $\mathcal{E}_{\rm t}$ at large $\overline{\eta}$. Simulation parameters are $\overline{L}_x = \overline{L}_y = 2\pi$, $N_x = 64$, $N_y = 32$ and $\nu = 0.3$, with isotropic differential strain.

of this section, we consider this range of loading, defined by equation (31): we derive the features of the energy minimizers analytically and compare with numerical simulations.

A classical result of plate theory is that the stretching energy, associated with a stiffness $E\,h$ directly proportional to the small parameter h, becomes dominant over the bending energy whose stiffness $E\,h^3$ scales like the third power of h. As a result, thin plates subjected to significant load attempt to minimize their stretching energy in a first place (mathematically, this defines a penalization problem). Unless this is prevented by the boundary conditions or by the geometry, their center-surface adopts a profile close to a developable surface — this happens for instance in folds and d-cones analyzed by Lobkovsky (1996); Ben Amar and Pomeau (1997). Therefore, we expect the optimal film shapes to make the film stretching energy (25) vanish at dominant order:

$$\mathcal{E}_{\rm fs}(w \in \mathcal{Q} \cap \mathcal{R}) = \frac{Eh}{2\,(1-\nu^2)} \left(\frac{\langle g''^2\rangle\,\langle F^2\rangle}{4} + \left(\frac{\langle f'^2\rangle}{2} - \eta_x \right)^2 + \left(\frac{\langle f'^2\rangle\,\langle g'^2\rangle}{2} - \eta_y \right)^2 + 2\nu \left(\frac{\langle f'^2\rangle}{2} - \eta_x \right) \left(\frac{\langle f'^2\rangle\,\langle g'^2\rangle}{2} - \eta_y \right) \right).$$

The same argument will be used in the last companion paper where we study a family of developable patterns. For large differential strain η_x and η_y, there are two types of factors that become formally large in this expression, namely $(\langle f'^2\rangle/2 - \eta_x)^2$ and $(\langle f'^2\rangle\,\langle g'^2\rangle/2 - \eta_y)^2$. We conjecture that the functions $f(x)$ and $g(y)$ with lowest energy make these terms cancel:

$$\langle f'^2\rangle \approx 2\,\eta_x, \qquad \langle g'^2\rangle \approx \frac{\eta_y}{\eta_x}, \tag{32}$$

as this the best way to lower the energy of the system. The prediction (32) is confirmed by the numerical simulations shown in Fig. 6. In these simulations, the differential strain is isotropic, $\eta_x = \eta_y$ and so $\langle g'^2\rangle$ is expected to converge to 1 for large $\overline{\eta}_x = \overline{\eta}_y$.

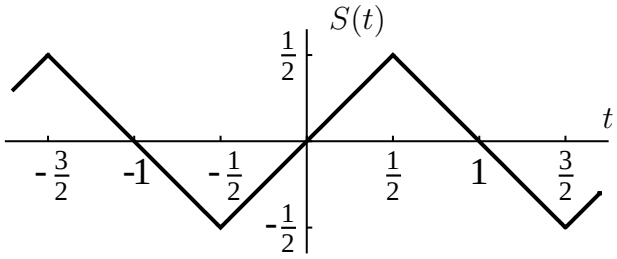

Fig. 7. Sawtooth function, as defined by equation (34).

6.2 Optimal film profile

We are left with one single term in the stretching energy, proportional to $\langle F^2 \rangle$. The function F has been defined in equation (15) as the antiderivative of $f'^2 - \langle f'^2 \rangle$. In order to minimize $\langle F^2 \rangle$, the function f should be such that $f'^2(x) \approx \langle f'^2 \rangle$ almost everywhere. Combining with equation (32), this yields

$$f'^2(x) \approx 2\,\eta_x \quad \text{for almost all } x.$$

The solutions for this equation are sawtooth functions, with slope $\pm\sqrt{2\,\eta_x}$. One possibility is that the sign of f' change periodically, as happens with the following function:

$$f(x) \to (2\,\eta_x)^{1/2}\,\ell_x\,S\left(\frac{x}{\ell_x}\right), \tag{33}$$

where ℓ_x is half the wavelength, a free parameter of the solution. In this equation, we have introduced the sawtooth function with period 2,

$$S(t) = \begin{cases} -1-t & \text{if } -1 \le t \le -1/2, \\ t & \text{if } -1/2 \le t \le 1/2, \\ 1-t, & \text{if } 1/2 \le t \le 1, \end{cases} \tag{34}$$

extended by periodicity for all t by $S(t+2) = S(t)$

This function is plotted in Fig. 7.

Equation (33) is not the only possibility for $f(x)$ as one can replace S by an irregular function $\tilde{S}$ such that $|\tilde{S}'(u)| = 1$ almost everywhere. Irregular sawtooth functions are likely to be less favorable as their bending energy is unevenly distributed across the film area, but they may well lead to metastable energy minima. The convergence of $f(x)$ towards the profile predicted by equation (33) has been observed in the simulations, see Fig. 8, left, with appropriate initial data [6]. We shall limit ourselves to formal arguments, without attempt-

[6] $f(x)$ converges to the regular sawtooth $S(x)$ when the load is gradually increased past the secondary threshold $\eta_c'^I$, following the procedure discussed in Section 7. If the simulation is started with a arbitrary value of the differential strain, $f(x)$ converges to an irregular sawtooth $\tilde{S}$.

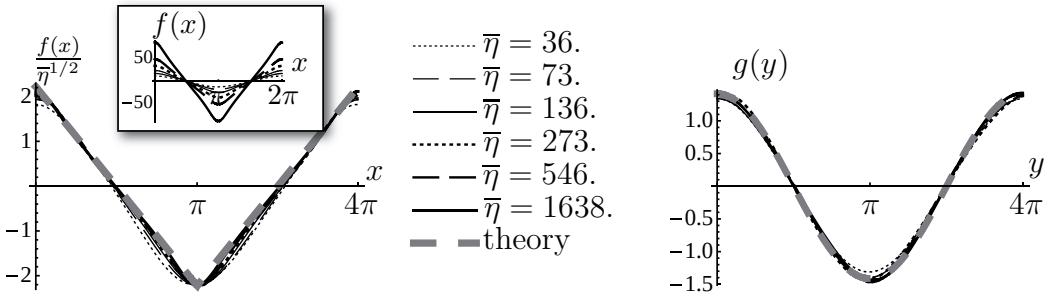

Fig. 8. Numerical confirmation of the convergence of the functions $f(x)$ and $g(y)$ to the profiles given by equations (33-35) for large $\overline{\eta}$. The parameters of the simulation are the same as in Fig. 6.

ing to establish the convergence by rigorous arguments.

In order to derive the function $g(y)$ in this limit of large applied loading, we shall first assume that $\langle F^2 \rangle$ converges to a nonzero value, a hypothesis that will be checked to be consistent at the end. The optimization problem for g is that the remaining term in the stretching energy, namely $\langle g''^2 \rangle \langle F^2 \rangle$, is minimum under the constraint $\langle g'^2 \rangle = \eta_y / \eta_x$ coming from equation (32). Technically, this constrained minimization problem can be solved using a Lagrange multiplier μ, and we seek the minimum of the functional

$$\int g''^2 \mathrm{d}y - \mu \int g'^2 \mathrm{d}y.$$

The corresponding Euler-Lagrange condition is the differential equation $g''''(y) + \mu g''(y) = 0$; its bounded solutions are harmonic [7] functions, up to an additive constant that is unimportant as it corresponds to a translation of the pattern along the x axis. For a similar reason, we fix the phase of the function $g(y)$ arbitrarily, as it corresponds to a translation of the pattern along the y axis. This yields, in the limit of large differential strain:

$$g(y) \to \left(2 \frac{\eta_y}{\eta_x} \right)^{1/2} \ell_y \sin \left(\frac{y}{\ell_y} \right). \tag{35}$$

Here, ℓ_y is the typical lengthscale for g, which is another free parameter of the solution. The convergence of $g(y)$ towards the profile predicted by equation (35) is again confirmed by numerical simulations, see Fig. 8, right.

At large differential strain, the minimizers of our simplified model are given by a sinusoidal function $f(x)$ and a sawtooth function $g(y)$, see equations (33) and (35). From equation (12), the function f determines the profile of the film when cut along a vertical plane perpendicular to the average direction of the ridges, although the graph of $g(y)$ yields the shape of the crest and valleys

[7] For negative μ, we also have solutions in the form of hyperbolic sine and cosine functions but the latter are not bounded and so are discarded.

of the pattern. Therefore, the optimal pattern at large load in the quasi-1D model is a developable surface obtained by folding a cylindrical shape along sinusoidal ridges, similar to that shown in Fig. 2d.

6.3 Energy of the minimizers, width of the ridges

This argument can be pushed further: by studying in more detail what happens near the angular points for $f(x)$, we shall be able to estimate the energy of the minimizers at large differential strain. The sawtooth profile (33) for $f(x)$ is unphysical near the angular points, where the bending energy diverges. There is a small layer near these angular points where bending has to be taken into account. This results in a profile that is regularized over a typical length δ much smaller than ℓ_x. This length δ is similar to the width of circular ridge studied by Pogorelov (1988). We shall estimate the ridge width δ along with the total energy of the film for the problem at hand.

In the layer obtained by regularizing the angular points, which we call the *ridge*, the order of magnitude of f' is, like everywhere, ${\eta_x}^{1/2}$. The second derivative f'' is zero far from the ridges where f has a linear dependence on x; across a ridge, f' changes sign, and so varies by an amount comparable to ${\eta_x}^{1/2}$ over a length δ. This yields the estimate $f'' \sim {\eta_x}^{1/2}/\delta$ in the ridge region. As f'' is nonzero over a fraction δ/ℓ_x of the x axis, the average of its square is estimated as

$$\langle f''^2 \rangle \sim \left(\frac{{\eta_x}^{1/2}}{\delta}\right)^2 \frac{\delta}{\ell_x} \sim \frac{\eta_x}{\delta\,\ell_x}. \tag{36}$$

From this equation, we find that the bending energy (26) is of order:

$$\mathcal{E}_{\text{fb}} \sim D\,\langle f''^2 \rangle \sim \frac{D\,\eta}{\delta\,\ell_x}. \tag{37}$$

For simplicity, we assume from now on that the differential strain is not severely anisotropic, *i. e.* that η_x and η_y have the same order of magnitude, called η: we write $\eta \sim \eta_x \sim \eta_y$.

Let us come back to the remaining term in the stretching energy (26), which is proportional to $\langle g''^2\rangle\langle F^2\rangle$. The factor $\langle g''^2\rangle$ can be estimated easily, as equation (32) implies that g' is a quantity of order 1. As a result, g'' is comparable to $1/\ell_y$, where ℓ_y is the typical length over which the smooth function $g(y)$ varies, and $\langle g''^2\rangle \sim {\ell_y}^{-2}$. In order to estimate the other factor, $\langle F^2\rangle$, we note that F is defined as the antiderivative of $f'^2 - \langle f'^2\rangle$, a quantity which is zero everywhere, except in the ridge regions, of length δ, where it is comparable to η. This yields

$$F \sim \delta\,\eta.$$

Combining these results, we estimate the first term in the stretching energy as

$$\langle g''^2 \rangle \, \langle F^2 \rangle \sim \frac{\delta^2 \, \eta^2}{{\ell_y}^2} \tag{38}$$

Note in passing that we can validate the initial and main assumption of our reasoning: if equation (32) were not satisfied, the stretching energy would be of order $Eh\,\eta^2$; when it is satisfied, it is of order $Eh\,\eta^2\,(\delta/\ell_y)^2$ by the calculation above. Anticipating on the fact that $\delta \ll \ell_y$, something that we shall check in the end, we confirm the fact that the constraints (32) allow a drastic decrease in the stretching energy, by a factor $(\delta/\ell_y)^2$.

We have just shown that the stretching energy of the film is comparable to

$$\mathcal{E}_{\rm s} \sim Eh \langle g''^2 \rangle \, \langle F^2 \rangle \sim Eh \, \frac{\delta^2 \, \eta^2}{{\ell_y}^2}. \tag{39}$$

The ridge width δ results from a balance of two antagonistic effects. The stretching energy above is lower when δ is smaller, although the bending energy (37) is lower when δ is larger. Balancing these two terms, we obtain an estimate for this width:

$$\frac{\delta}{\ell_y} \sim \left(\frac{h^2}{\ell_x \ell_y \eta} \right)^{1/3}. \tag{40}$$

Noting $\lambda = 2\pi/k = 2\pi \, h^* \, C^{1/3}$ the wavelength of the initial, cylindrical buckling pattern, and rescaling the in-plane lengths ℓ_x and ℓ_y using λ, we have

$$\overline{\ell}_x = \frac{\ell_x}{\lambda} \sim \frac{\ell_x}{h \, C^{1/3}}, \qquad \overline{\ell}_y = \frac{\ell_y}{\lambda} \sim \frac{\ell_y}{h \, C^{1/3}}. \tag{41}$$

Recalling the definition (29) of the rescaled differential strain, we rewrite the estimate for δ given above in equation (40) in terms of dimensionless quantities:

$$\frac{\delta}{\ell_y} \sim \frac{1}{\left(\overline{\ell}_x \, \overline{\ell}_y \, \overline{\eta} \right)^{1/3}}. \tag{42}$$

This expression confirms that the ridge width is small compared to the wavelength ℓ_y in the strongly nonlinear limit, $\overline{\eta} \gg 1$, assuming that the wavelengths of the pattern are comparable to the wavelength λ of the stripe pattern at the onset of bifurcation threshold ($\ell_{x,y} \sim \lambda$ implies $\overline{\ell}_{x,y} \sim 1$). This makes our approach consistent.

With the ridge width given in equation (42), the stretching energy (39) and bending energy of the film are both of the same order of magnitude, and the total energy of the film reads

$$\mathcal{E}_{\rm f} \sim Eh \left(\frac{h^2}{\ell_x \ell_y} \right)^{2/3} \eta^{4/3} = Eh \, \frac{\overline{\eta}^{4/3}}{C^{4/3} \, (\overline{\ell}_x \, \overline{\ell}_y)^{2/3}}. \tag{43}$$

We shall now show that the energy of the substrate is negligible, that is much smaller than $\mathcal{E}_\mathrm{f}$ in this limit. The typical deflection w is found from equation (33) as $w \sim f \sim \eta^{1/2}\,\ell_x$, whereas the wavevector k that brings the dominant contribution to the substrate energy is $1/\min(\ell_x, \ell_y)$. Plugging this into the definition (8) of the substrate energy yields

$$\mathcal{E}_\mathrm{s} \sim E_\mathrm{s}\,\eta\,\frac{{\ell_x}^2}{\min(\ell_x, \ell_y)}.$$

The ratio of this substrate energy to the film energy (43) reads

$$\frac{\mathcal{E}_\mathrm{s}}{\mathcal{E}_\mathrm{f}} \sim \left(\frac{\overline{\ell_x}^{8/3}\,\overline{\ell_y}^{2/3}}{\min(\overline{\ell}_x, \overline{\ell}_y)}\right)\,\frac{1}{\overline{\eta}^{1/3}}. \tag{44}$$

Whenever the right-hand side in equation (44) is small, the energy of the substrate is negligible, $|\mathcal{E}_\mathrm{s}| \ll |\mathcal{E}_\mathrm{f}|$, and the total energy is estimated as:

$$\mathcal{E}_\mathrm{t} \sim \mathcal{E}_\mathrm{f}\ \sim Eh\,\frac{\overline{\eta}^{4/3}}{C^{4/3}\,(\overline{\ell}_x\,\overline{\ell}_y)^{2/3}}, \quad \text{provided } \frac{\overline{\ell_x}^{8/3}\,\overline{\ell_y}^{2/3}}{\min(\overline{\ell}_x, \overline{\ell}_y)} \ll \overline{\eta}^{1/3}. \tag{45}$$

This happens in particular in the limit of large load, $\overline{\eta} \gg 1$, when the pattern wavelengths are comparable to the buckling wavelength λ at the onset of bifurcation — then, $\overline{\ell}_x$ and $\overline{\ell}_y$ are of order unity.

The main result of this scaling analysis of the ridge is that the total energy of the pattern goes like $\overline{\eta}^{4/3}$ at large differential strain, when all the other parameters remain unchanged, see equation (45). We have confirmed this scaling behavior with the numerical simulations shown in Fig. 6, right. In this figure, the numerical value of $\langle f''^2\rangle$ at large $\overline{\eta}$ is also compared to a prediction that can be made by combining equations (36) and (40), namely $\langle f''^2\rangle \sim \eta^{4/3}$, and a good agreement is found.

6.4 Tentative prediction of wavelengths based on energy minimization

It is interesting to optimize the energy (45) of the pattern with respect to its wavelengths, ℓ_x and ℓ_y. The result is somewhat surprising as we shall now show that the optimal rescaled wavelengths are $\overline{\ell}_x \to 0$ and $\ell_y \to \infty$. Indeed, let us introduce a large number, ρ, which will soon be identified with the aspect ratio $\overline{\ell}_y/\overline{\ell}_x \gg 1$ of the pattern, and consider wavelengths that scale like $\overline{\ell}_y \sim (\overline{\eta})^{1/7}\,\rho^\gamma$ and $\overline{\ell}_x \sim (\overline{\eta})^{1/7}/\rho^{1-\gamma}$, where γ is a number in the range $\gamma \in [\frac{1}{2}, \frac{5}{7}]$. By plugging these expressions into equation (45), we find that the energy scales like $\mathcal{E}_\mathrm{t} \sim E\,h\,C^{-4/3}\,\overline{\eta}^{24/21}/\rho^{\frac{4}{3}\left(\gamma-\frac{1}{2}\right)}$ and therefore goes to zero

at fixed $\overline{\eta}$ when $\rho \to \infty$, given that $\gamma > \frac{1}{2}$. The condition on the right-hand side of equation (45) is satisfied provided $1/\rho^{\frac{5-7\gamma}{3}} \to 0$, and this is indeed the case with $\gamma < \frac{5}{7}$. We have shown that the pattern that achieves the absolute minimum of energy is made of curvilinear ridges with $\ell_x \ll \ell_y$: the spacing between ridges is much smaller than than the wavelength of these sinusoidal ridges. A similar oddity will be obtained with the full model (Audoly and Boudaoud, 2007c). In contrast, the two wavelengths of the pattern are comparable in the experiments. This points to the fact that the wavelengths of the pattern are not selected by energy minimization at large load but instead by a trapping mechanism, as explained in Section 7.

6.5 On the shape of crests and valleys

At large load, we have found that the quasi-1D model predicts a developable pattern made of piecewise cylindrical shapes connected by sinusoidal ridges, as in Fig. 2d. In the last companion paper, we shall show that the exact model predicts a similar pattern in this limit, but with zigzag crests and valleys comprising angular points. This discrepancy concerning the shape of crests and valleys is caused by the kinematical assumptions at the basis of the quasi-1D model, as discussed in detail in the forthcoming paper. Although it does not predict the correct ridge shapes, the quasi-1D model shows how undulating patterns, obtained by a sequence of two buckling bifurcation, progressively evolve towards a piecewise developable shape. Even more importantly, this approximate models explains how the wavelengths of the pattern are selected, as investigated in the next Section.

7 Selection of wavelength, metastability and trapping

In our simulations of the quasi-one dimensional model, the differential strain is progressively increased from zero. As explained in Section 5, we observe a bifurcation to a straight stripe pattern which becomes unstable towards an undulating zigzag pattern — sometimes, the stripe pattern is not observed at all as the system jumps directly to the zigzag pattern, see Fig. 5. When the differential strain is further increased, the smooth undulating pattern evolves progressively into a pattern with sharp curvilinear ridges, as shown in the previous Section. When the loading is increased by small increments and the system is allowed to relax at each step, this smooth transition from undulating stripes to a developable pattern with ridges does not involve any noticeable change in the wavelengths of the pattern (this concerns both the wavelength along the average ridge direction and the spacing between neighboring ridges). As a result, the piecewise developable patterns obtained at the maximum

loading that the simulation can handle, typically $\overline{\eta} \sim 10^3$, have wavelengths close to $\lambda = 2\pi/k$, the wavelength of the cylindrical pattern at the onset of buckling.

In contrast, we argued in Section 6.4 that the pattern with lowest energy is a piecewise developable shape having widely different longitudinal and transverse wavelengths: its inter-crest spacing is much smaller than λ, although the wavelength of the crests (and valleys) is much larger than λ. This points to the fact that the system has many local equilibrium configurations and that it is unable to pick that with lowest energy in the simulation. In the presence of a small amount of dissipation, or when the dimension of the film is large but finite, the wavelength of a pattern cannot not vary smoothly but by jumps, by a local doubling of wavelength for instance. As a result, the system is able to explore a limited set of wavelengths only. Consequently, the wavelength is frozen during loading, and remains comparable to its value λ at the onset of buckling. We claim that the wavelengths observed at relatively large buckling number in the experiments result from this trapping mechanism, and not from a principle of energy minimization.

In the present section, we provide numerical evidence of this trapping mechanism and show that a pattern keeps its wavelengths and overall geometry unchanged (unless severely perturbed) even though they are no longer the ones with lowest energy. The simulations presented in this section are carried out on a domain several times larger than the initial wavelength of the instability, and so the unit simulation cell comprises many wavelengths of the pattern.

In Fig. 9, we illustrate the existence of several local equilibria by showing two numerical equilibria observed in the same loading conditions but following different loading histories. In the upper part of the figure, the pattern has been obtained with a slowly increasing loading and the resulting pattern is periodic. In the lower part of the figure, it has been obtained with a non-monotonic loading varied by jumps; the resulting pattern is not periodic along the y direction. The two patterns correspond to the same set of final parameters. There are five wavelengths across the width of the unit cell in the first case, and seven in the second case. This illustrates the dependence of the pattern on the loading history, and the existence of many local equilibria.

This trapping mechanism is clearly demonstrated by the simulations shown in Fig. 10. The simulation is started with a differential strain $\overline{\eta}$ a few times above the primary threshold, typically $\overline{\eta} \approx 5$. Differential strain is then increased smoothly. As explained earlier, the herringbone pattern obtained in this way has periodic crests (or valleys) with a wavelength close to the initial buckling wavelength λ. The spacing between these crests and valleys is of the same order of magnitude. When $\overline{\eta}$ is further increased, the geometry of the pattern

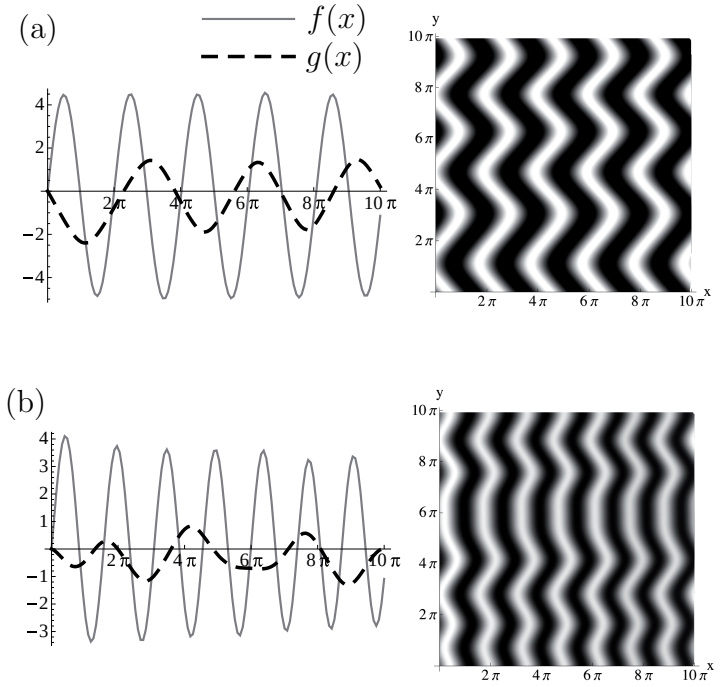

Fig. 9. Existence of multiple equilibria with identical parameters and loading. For both simulations, the parameters are $N_x = N_y = 128$, $\ell_x = \ell_y = 10\pi$, $\nu = .3$ and $\overline{\eta} = 6.36$ (a) $\overline{\mathcal{E}}_{\rm t} = -31.9$ (b) $\overline{\mathcal{E}}_{\rm t} = -23.1$. Note the difference in wavelengths.

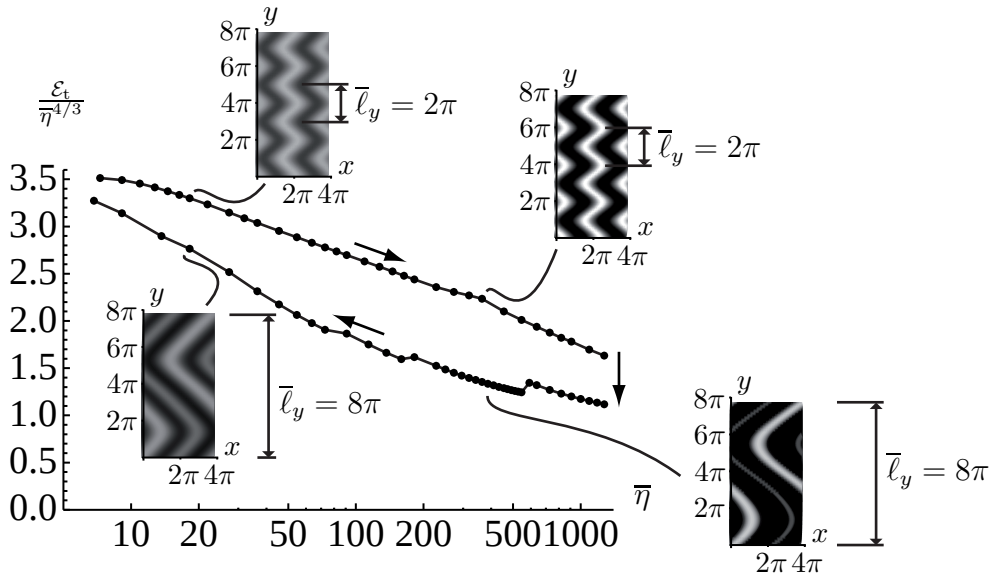

Fig. 10. Tracking of numerical solutions for a loading cycle. The system is 'shaken' at the maximum loading to allow better relaxation of the energy, and jumps to a pattern with large wavelengths. The energy is plotted along this loading cycle, revealing a hysteresis: under increasing loading, the numerical solution is trapped in a local minimum of energy. Simulation parameters are $L_x = 4\pi$, $L_y = 8\pi$, $N_x = 32$, $N_y = 64$, $\nu = .3$

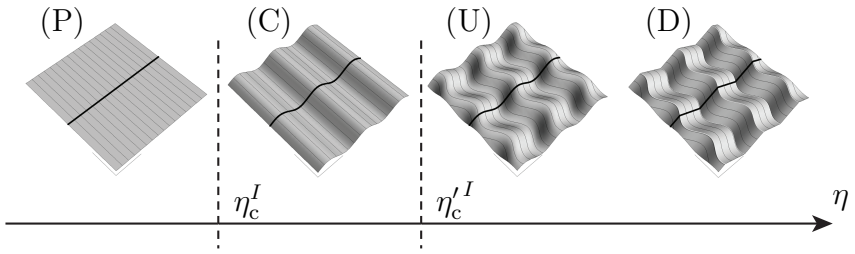

Fig. 11. Summary of patterns under increasing load η. (P) flat, unbuckled state, (C) straight wrinkles (cylindrical state), (U) undulating stripes, (D) Developable pattern. The transitions from P to C and from P to U correspond to the primary and secondary buckling at well-defined thresholds in compressive strain, whereas the evolution from U to D is smooth. Pattern D has curvilinear ridges in the quasi-1D model (see Section 6) but piecewise straight zigzag ridges in the full model (see analysis of the Miura-ori pattern in the last companion paper).

changes very little, and none of the wavelengths varies noticeably (see insets on top of Fig. 10); the only difference is that the pattern has a higher and higher contrast as the deflection of the film increases. However, if the simulation is reset to an almost flat configuration at large strain $\overline{\eta}$, of the order of 1000, the inter-crest spacing and longitudinal wavelength jump to the largest accessible value, *i.e.* to the size of the simulation cell L_x and L_y. This is consistent with the fact that the energy (45) decreases when the wavelengths ℓ_x or ℓ_y increase [8]. When the loading $\overline{\eta}$ is decreased from there, down to values as small as $\overline{\eta} \sim 5$, the wavelengths do not change either. We have computed the energy along these two branches and found that the second pattern always has a significantly lower energy that the first one. This means that the solution obtained under increasing loading has remained trapped in a local equilibrium configuration all the way up to the maximum applied loading, $\overline{\eta} \sim 10^3$.

The numerical observations in Fig. 10 confirm the findings of Section 6.3, namely that the optimal wavelengths are widely different from the wavelength λ at the onset of buckling. When the residual stress is gradually increased, the pattern is not selected by global energy minimization: the transverse and longitudinal wavelengths of a herringbone pattern remain locked in a metastable minimum under increasing load. In the experiments, they are probably fixed by the initial and secondary buckling bifurcations, leading to undulating patterns.

8 Conclusion

In this paper, we investigated the formation of herringbone patterns in compressed thin films bonded to a compliant substrate, based on a simplified buckling model. This model is built by imposing kinematical constraints on the film shape. These kinematical constraints were chosen so as to be compatible with analytical solutions of the problem available in the limits of small and large loads — the patterns such as the checkerboard that are unrelated to the formation of herringbones, are not included in the present analysis. This reduced model has the remarkable property that its stretching energy vanishes whenever the actual stretching energy vanishes; as a result, smooth developable surfaces are favored in the limit of large compression, as in the exact model. A validation is provided by comparison of the results of a linear stability analysis and of a weakly nonlinear analysis, based either on the simplified or exact models. A similar buckling model has been used to analyze multiscale, self-similar buckling patterns in thin elastic plates (Audoly and Boudaoud, 2003), and might be applicable to other buckling problems.

Using numerical simulations of the simplified model, we recovered the initial and secondary buckling bifurcations, first to a cylindrical pattern and second to an undulating pattern. The undulating pattern evolves smoothly towards a developable pattern with ridges at large differential strain. This developable pattern is very similar to the Miura-ori pattern analyzed in the last companion paper, and to the experimental herringbone patterns; a minor difference, coming from the approximations introduced, is that the numerical minimizers have curved — and not sawtooth-like — crests and valleys in the quasi-1D model. By the developability condition, the ratio of principal residual stresses can be extracted from the profile $g(y)$ of the crests and valleys; see equation (32).

Our numerical simulations reveal that many equilibrium states are possible. When the compressive strain is gradually increased, the system remains trapped in a local minimum of energy which is not the global one. As a result, the longitudinal and transverse wavelengths of herringbone patterns in real experiments are expected to be comparable to the buckling wavelength λ at threshold; the precise value of its aspect ratio depends on the detailed history of loading at the early stage of the experiment.

Our results are in qualitative agreement with the experiments showing herringbone patterns under approximately isotropic compression, by Bowden et al. (1998) and Huck et al. (2000), and with the numerical simulations based on

[8] Note that we do not obtain a pattern with a large aspect ratio $\ell_y \gg \ell_x$ after the jump, as could be expected from the analysis of Section 6.4. This is probably because the system has jumped to metastable state with a lower energy that is still not the absolute energy minimum.

the finite elements method by Chen and Hutchinson (2004) on the unit cell of a periodic pattern. More specifically, we have rationalized the following observations. The existence of many metastable states accounts for the variability of patterns in the experiments, as well as for the weak dependence of the energy on the aspect ratio of the pattern in the simulations. The proposed trapping mechanism accounts for the fact that the longitudinal wavelength of the zigzags and the gap between them are comparable.

The simplified model allows one to propose a global scenario for the evolution of the pattern, from undulating stripes to developable surfaces with ridges, reminiscent of herringbones. This scenario accounts for many previous experimental and numerical observations, except for the fact that, the profile of the ridges is sinusoidal in the approximate model, unlike in the experiments. This discrepancy will be resolved in the last companion paper (Audoly and Boudaoud, 2007c), where exact solutions of the original equations are derived in the limit of large buckling parameter.

References

Allen, H. G., 1969. *Analysis and Design of Structural Sandwich Panels*. Pergamon Press, New York.

Audoly, B., Boudaoud, A., 2003. Self-similar structures near boundaries in strained systems. Phys. Rev. Lett. 91, 086105.

Audoly, B., Boudaoud, A., 2007a. Buckling of a thin film bound to a compliant substrate (part I). Formulation, linear stability of cylindrical patterns, secondary bifurcations. Submitted to Journal of the Mechanics and Physics of Solids.

Audoly, B., Boudaoud, A., 2007c. Buckling of a thin film bound to a compliant substrate (part III). Herringbone solutions at large buckling parameter. Submitted to Journal of the Mechanics and Physics of Solids.

Ben Amar, M., Pomeau, Y., 1997. Crumpled paper. Proceedings of the Royal Society A: Mathematical, Physical and Engineering Sciences 453, 729–755.

Bowden, N., Brittain, S., Evans, A. G., Hutchinson, J. W., Whitesides, G. M., 1998. Spontaneous formation of ordered structures in thin films of metals supported on an elastomeric polymer. Nature 393, 146–149.

Chen, X., Hutchinson, J. W., 2004. Herringbone buckling patterns of compressed thin films on compliant substrates. Journal of Applied Mechanics 71, 597–603.

Genzer, J., Groenewold, J., 2006. Soft matter with hard skin: from skin wrinkles to templating and material characterization. Soft Matter 2, 310–323.

Huang, Z., Hong, W., Suo, Z., 2004. Evolution of wrinkles in hard films on soft substrates. Physical Review E (Statistical, Nonlinear, and Soft Matter Physics) 70, 030601.

Huang, Z. Y., Hong, W., Suo, Z., 2005. Nonlinear analyses of wrinkles in a film bonded to a compliant substrate. Journal of the Mechanics and Physics of Solids 53, 2101–2118.

Huck, W., Bowden, N., Onck, P., Pardoen, T., Hutchinson, J., Whitesides, G., 2000. Ordering of spontaneously formed buckles on planar surfaces. Langmuir 16, 3497–3501.

Jin, W., Sternberg, P., 2001. Energy estimates for the von Kàrmàn model of thin-film blistering. Journal of Mathematical Physics 42, 192–199.

Lobkovsky, A. E., 1996. Boundary layer analysis of the ridge singularity in a thin plate. Physical Review E (Statistical, Nonlinear, and Soft Matter Physics) 53, 3750–3759.

Pogorelov, A. V., 1988. *Bendings of surfaces and stability of shells*. No. 72 in Translation of mathematical monographs. American Mathematical Society.

Timoshenko, S., Gere, J. M., 1961. *Theory of elastic stability*. MacGraw Hill, New York, 2$^{\text{nd}}$ edn.

Yoo, P. J., Suh, K. Y., Park, S. Y., Lee, H. H., 2002. Physical self-assembly of microstructures by anisotropic buckling. Advanced materials 14, 1383–1387.